

# Mars Entry Atmospheric Data System Modelling and Algorithm Development

Christopher D. Karlgaard\*, Roger E. Beck†, Stephen A. O'Keefe‡,  
Paul M. Siemers, III§, Brady A. White¶  
*Analytical Mechanics Associates, Inc.*

Walter C. Engelund|| and Michelle M. Munk\*\*  
*NASA Langley Research Center*

The Mars Entry Atmospheric Data System (MEADS) is being developed as part of the Mars Science Laboratory (MSL), Entry, Descent, and Landing Instrumentation (MEDLI) project. The MEADS project involves installing an array of seven pressure transducers linked to ports on the MSL forebody to record the surface pressure distribution during atmospheric entry. These measured surface pressures are used to generate estimates of atmospheric quantities based on modeled surface pressure distributions. In particular, the quantities to be estimated from the MEADS pressure measurements include the total pressure, dynamic pressure, Mach number, angle of attack, and angle of sideslip. Secondary objectives are to estimate atmospheric winds by coupling the pressure measurements with the on-board Inertial Measurement Unit (IMU) data. This paper provides details of the algorithm development, MEADS system performance based on calibration, and uncertainty analysis for the aerodynamic and atmospheric quantities of interest. The work presented here is part of the MEDLI performance pre-flight validation and will culminate with processing flight data after Mars entry in 2012.

## I. Introduction

The Mars Entry, Descent, and Landing Instrumentation (MEDLI) system is an array of sensors installed in the heat shield of the Mars Science Laboratory (MSL) entry vehicle. The goals of this project are to measure the aerodynamic and aerothermal environment during atmospheric entry.<sup>1</sup> The MEDLI system consists of three basic subsystems: The Mars Integrated Sensor Plug (MISP), the Mars Entry Atmospheric Data System (MEADS), and the Sensor Support Electronics (SSE). The MISP system uses 7 sensor plugs installed in the heat shield, each plug consisting of 1 recession sensor and 4 thermocouple sensors, to measure the aerothermal environment during entry. MEADS makes use of 7 flush pressure measurements on the aeroshell fore-body to allow estimation of atmospheric state parameters, and when combined with external velocity measurements, atmospheric parameters such as density and winds. The SSE is an electronics box that provides the signal conditioning and data acquisition systems for MISP and MEADS. This paper is focused on the development of models and algorithms in support of MEADS system design and, eventually, flight data processing. Details on the MEADS subsystem requirements and design are provided in Ref. 2. Information on other MEDLI instruments can be found in Ref. 1.

The basic MEADS science objectives are to reconstruct atmospheric data variables from pressure measurements alone when the freestream dynamic pressure is above 850 Pa. In particular, the objectives are to estimate the angles of attack and sideslip to within 0.5 deg, the dynamic pressure to within 2%, and the Mach number to within 0.1, in a  $3\sigma$  sense. These accuracy goals are based largely on flight experience

---

\*Senior Project Engineer, Analytical Mechanics Associates, Inc, Hampton, VA, AIAA Senior Member

†Senior Project Engineer, Analytical Mechanics Associates, Inc, Huntsville, AL, AIAA Member.

‡Project Engineer, Analytical Mechanics Associates, Inc, Hampton VA

§Consultant

¶Project Engineer, Analytical Mechanics Associates, Inc., Hampton VA, AIAA Member

||Head, Atmospheric Flight and Entry Systems Branch, AIAA Associate Fellow

\*\*MEADS System Lead, Atmospheric Flight and Entry Systems Branch, AIAA Senior Member

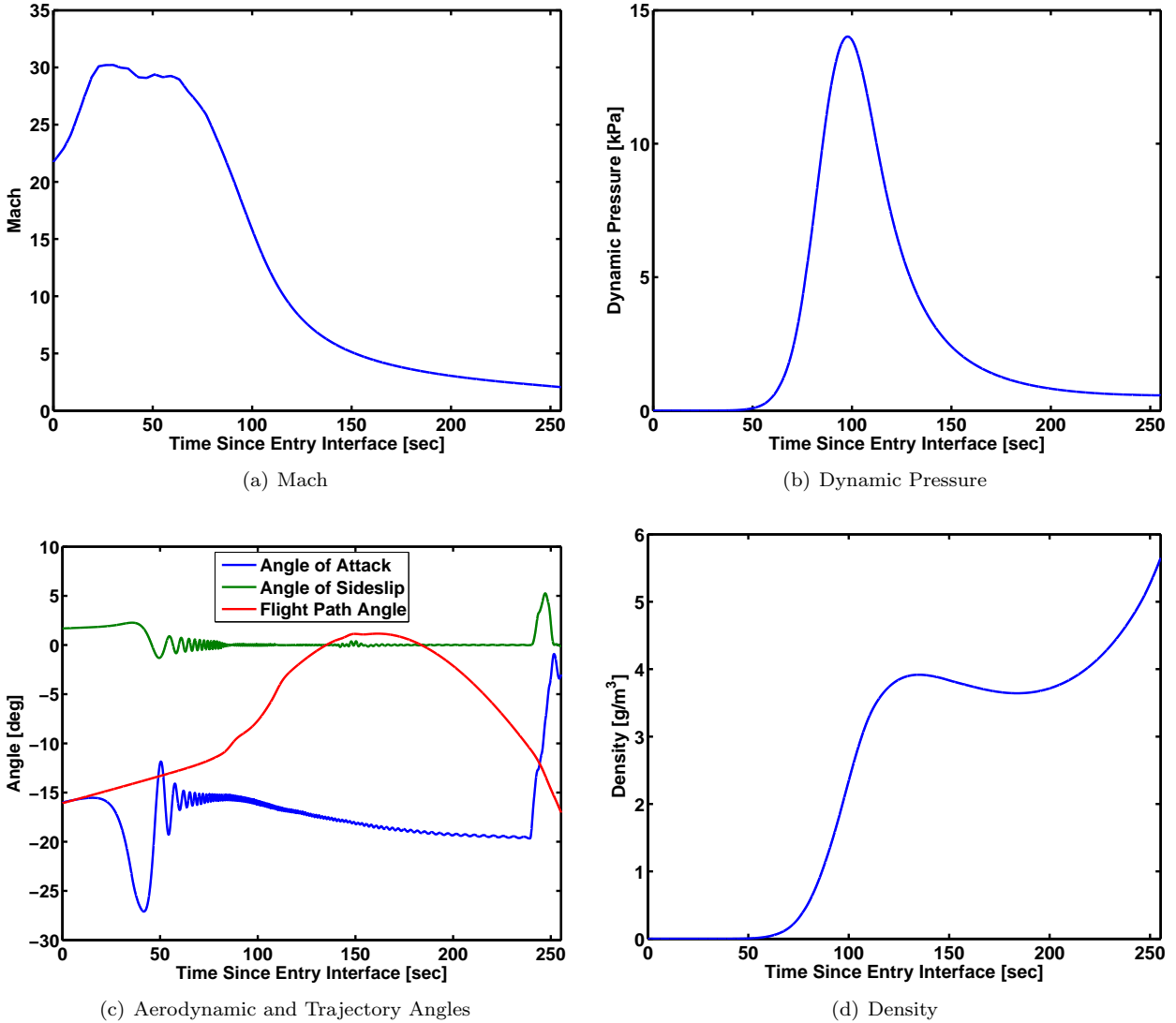
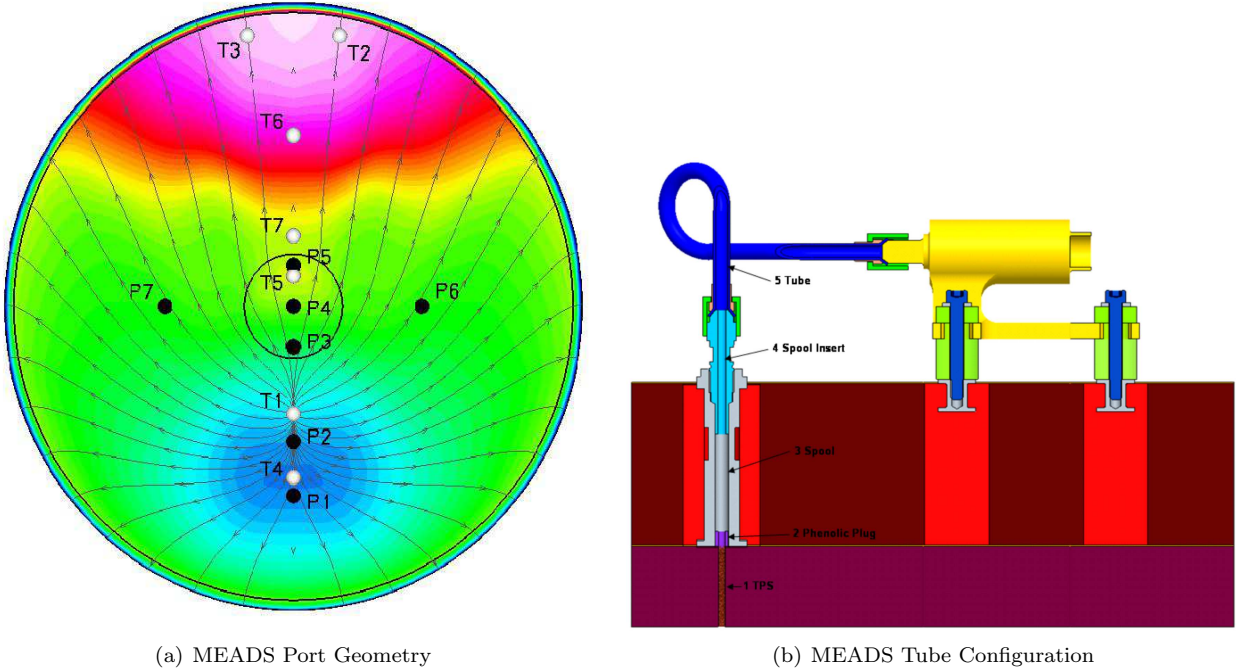


Figure 1. MSL Reference Trajectory

with the Shuttle Entry Air Data System (SEADS).<sup>3-5</sup> Secondary objectives are to estimate the freestream density and atmospheric winds from the MEADS pressure measurements, when combined with the on-board Inertial Measurement Unit (IMU) data. These measurements will aid the MSL trajectory reconstruction and performance analysis, and will separate the aerodynamic and atmospheric uncertainties.

Seven pressure ports are proposed for the MSL geometry as shown in Fig. 2(a), labelled as ports P1 through P7(MISP locations are shown as T1 through T7). As seen above, the angle of attack remains near 20 deg. over much of the trajectory. At these conditions the stagnation region is along the windward part of the cone and a recompression and potential for turbulent flow is predicted along the leeward side. To minimize the uncertainties in pressure measurements the proposed port layout avoids placing ports in the latter region.

Pressure ports P1 and P2 are located in the stagnation region to provide a nearly direct measurement of the total pressure at the high Mach regime. Ports P3, P4, and P5 lie on the spherical cap and are placed in order to take advantage of the simple geometry for angle of attack measurements. Additionally, P4, located at the geometric center, provides a nearly direct total pressure measurement at the low Mach regime prior to parachute deployment. The final two ports are located in the horizontal plane of symmetry, approximately 1.0 meters off of the centerline. The ports, P6 and P7, provide the off-axis measurements needed to estimate the angle of sideslip. The pressure ports are connected to pressure transducers via a tube system illustrated in Fig. 2(b). The measured pressures are sampled at a rate of 8 Hz from entry interface until heat shield separation.



**Figure 2. MEADS Geometry and Tube Configuration**

The remainder of the paper is organized as follows. Section II discusses the basic surface pressure distribution modelling. Section III discusses atmospheric data estimator design using least-squares and Kalman filtering techniques. Section IV provides a summary of error models, trade studies, and system performance analysis. Current status and future work plans are outlined in Sec. V.

## II. Pressure Models

### A. Newtonian Flow Model

In the traditional implementations of FADS-based air data estimation, the surface pressures are modelled using Newtonian flow approximations in which the surface pressure is a function of the port location, angle of attack, angle of sideslip, and Mach number. Explicitly, the surface pressure at port  $i$  is given by<sup>3</sup>

$$p_i = p_t [(1 - R) \cos^2 \theta_i + R] \quad (1)$$

where  $p_t$  is the total pressure,  $R$  is ratio of static pressure to total pressure, and  $\theta_i$  is the incidence angle. The pressure ratio is a function of the Mach number, which takes the form<sup>3</sup>

$$R = \frac{p_\infty}{p_t} = \begin{cases} \left[ \frac{2}{(\gamma+1)M_\infty^2} \right]^{\gamma/(\gamma-1)} \cdot \left[ \frac{2\gamma M_\infty^2 - (\gamma-1)}{\gamma+1} \right]^{1/(\gamma-1)} & \text{for } M_\infty > 1 \\ \left[ 1 + \frac{\gamma-1}{2} M_\infty^2 \right]^{-\gamma/(\gamma-1)} & \text{for } M_\infty \leq 1 \end{cases} \quad (2)$$

The pressure ratio is shown as a function of Mach number for  $\gamma = 1.335$  in Fig. 3(a).

The incidence angle is a function of the port location and angles of attack and sideslip, given by

$$\cos \theta_i = \cos \alpha \cos \beta \cos \lambda_i + \sin \beta \sin \phi_i \sin \lambda_i + \sin \alpha \cos \beta \cos \phi_i \sin \lambda_i \quad (3)$$

where  $\lambda_i$  is the cone angle and  $\phi_i$  is the clock angle of the orifice.

Substituting Eqs. (2–3) into Eq. (1) yields a relationship for surface pressure as a function of the port location, total pressure, Mach number, and angles of attack and sideslip. The Newtonian flow pressure model can also be written as a function of the freestream dynamic pressure by making use of the relationship<sup>3</sup>

$$q_\infty = \left( \frac{\gamma}{2} \right) p_t R M_\infty^2 \quad (4)$$

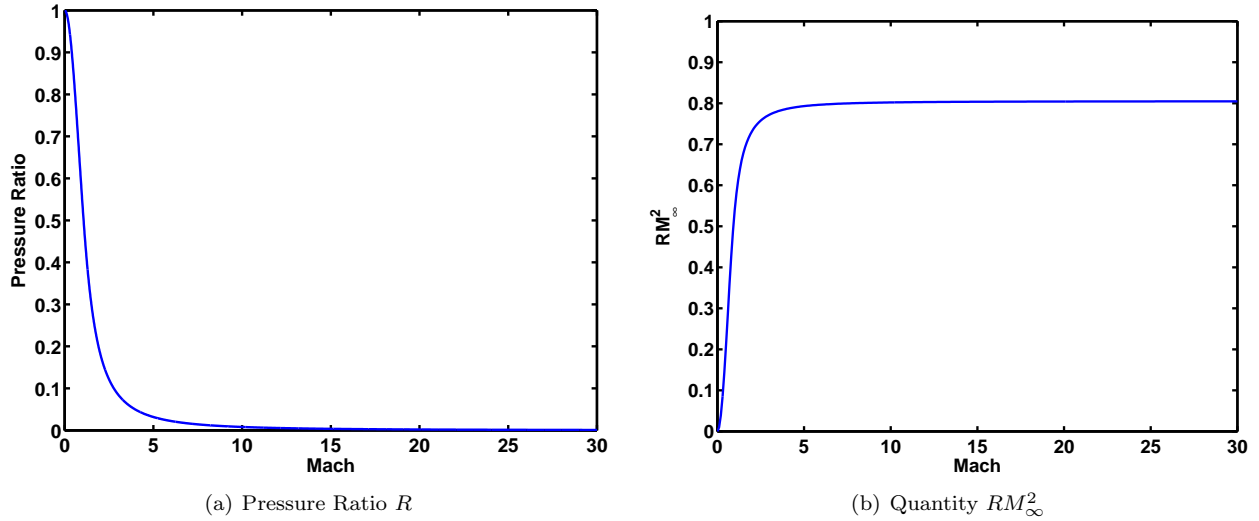


**Figure 3. Pressure Ratio vs. Mach for  $\gamma = 1.335$**

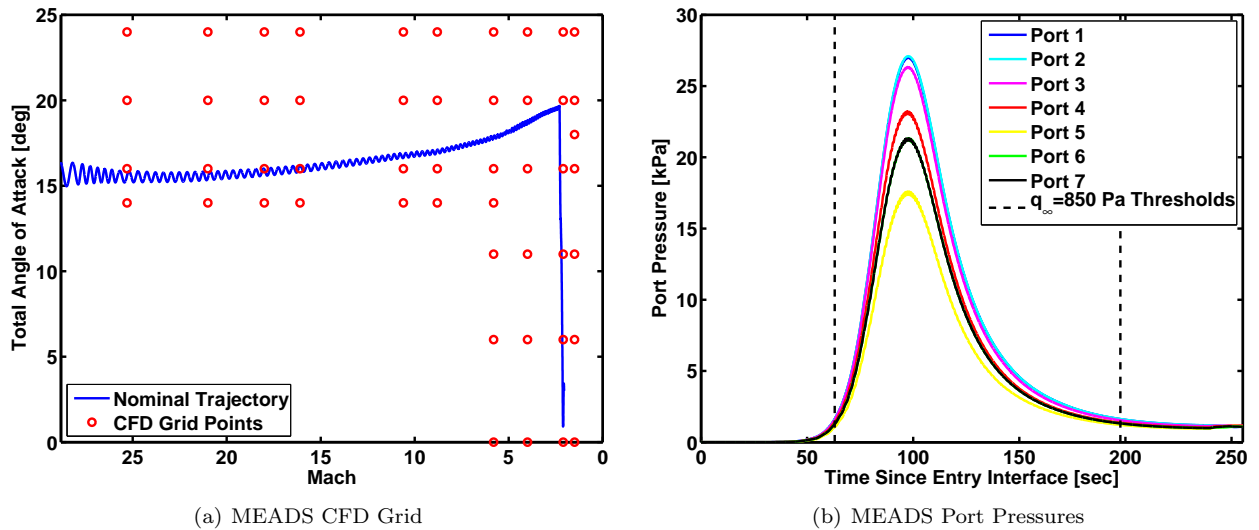


**Figure 4. MEADS CFD Grid and Port Pressure**

As noted in Ref. 3, 4, for small  $R$  (or, equivalently, high Mach) the product  $RM_{\infty}^2$  is nearly constant. This trend is illustrated in Fig. 3(b) for  $\gamma = 1.335$ . The implications of this trend are twofold. First, any slight change in static pressure has a large impact on the Mach number, which implies that the Mach number is difficult to estimate for low pressure ratios. Secondly, it implies that the dynamic pressure can be computed accurately directly from the total pressure by substituting the limiting value of the quantity  $RM_{\infty}^2$ . Therefore, errors in static pressure or Mach number do not contribute to errors in dynamic pressure estimates in the high hypersonic regime.

## B. CFD-Based Model

A CFD-based table lookup model was developed for analysis of the MSL air data system. This CFD database is based on supersonic and hypersonic regime pressure distributions from thin-layer Navier-Stokes solutions generated using the Langley Aerothermal Upwind Relaxation Algorithm (LAURA). The relaxation of vibrational temperature of the  $CO_2$  molecule is simulated using the CAMAC model. Forebody solutions were obtained using a 7 block singularity-free grid.

The supplied CFD database was converted from absolute pressure to pressure coefficient in order to allow the pressure distribution to scale with different trajectories and to enable estimation of freestream

atmospheric properties such as the static pressure. The data was re-interpolated from the 7 block grid to a single-zone grid of clock and cone angles. This alteration simplifies the interpolation of surface conditions without complications of search routines required to handle multiple zones.

The CFD grid points are shown as a function of total angle of attack and Mach number in Fig. 4(a) along with the nominal reference trajectory. The pressure profiles for each MEADS port are shown in Fig. 4(b). Note that each CFD grid point consists of a full surface pressure distribution solution, with 37 clock angles in uniform 5 deg increments and 61 cone angles with non-uniform increments. These grid points can be interpolated using linear or cubic spline techniques. The linear interpolation is significantly faster and is therefore suitable for Monte-Carlo analysis. Cubic interpolation is suitable for analyzing specific simulation cases or flight data.

### III. Atmospheric Data Estimation

The basic MEADS atmospheric state estimation procedure is essentially similar to the SEADS state estimation described in Ref. 3, a point-wise least squares fit of the surface pressure measurements to the modelled pressure distribution to determine minimum-variance estimates of the atmospheric states. When combined with an Inertial Measurement Unit (IMU), the MEADS measurements can also be used to generate wind and density estimates. This section describes the techniques used to estimate these quantities, beginning with the basic MEADS estimation technique to compute the atmospheric state variables.

#### A. Least-Squares State Variable Estimation

By defining the atmospheric state vector as  $\mathbf{x}$ ,  $\mathbf{p}$  as the vector of  $N$  observed surface pressures, and the pressure model as  $\mathbf{h}(\mathbf{x}, t)$  then the pressure measurement model can be written compactly as

$$\mathbf{p} = \mathbf{h}(\mathbf{x}, t_k) + \boldsymbol{\epsilon} \quad (5)$$

where  $\boldsymbol{\epsilon}$  is the vector of pressure measurement errors and  $t_k$  is the measurement sampling time. The pressure measurement model can be approximated by means of the truncated series expansion

$$\mathbf{p} \approx \mathbf{h}(\bar{\mathbf{x}}, t_k) + \mathbf{H}(t_k)(\mathbf{x} - \bar{\mathbf{x}}) + \boldsymbol{\epsilon} \quad (6)$$

where  $\bar{\mathbf{x}}$  is some reference state and  $\mathbf{H}(t_k)$  is the Jacobian matrix

$$\mathbf{H}(t_k) = \left[ \frac{\partial \mathbf{h}}{\partial \mathbf{x}} \right]_{\mathbf{x}=\bar{\mathbf{x}}} \quad (7)$$

The problem can be reduced to that of a linear regression problem

$$\mathbf{y} = \mathbf{H}\mathbf{x} + \boldsymbol{\epsilon} \quad (8)$$

where  $\mathbf{y} = \mathbf{p} - \mathbf{h}(\bar{\mathbf{x}}, t_k) + \mathbf{H}\bar{\mathbf{x}}$ . By virtue of the Gauss-Markov theorem, the best linear unbiased estimate of  $\mathbf{x}$  is the weighted least-squares solution,<sup>6</sup>

$$\hat{\mathbf{x}} = (\mathbf{H}^T \mathbf{R}^{-1} \mathbf{H})^{-1} \mathbf{H}^T \mathbf{R}^{-1} \mathbf{y} \quad (9)$$

where  $\mathbf{R}$  is the pressure measurement error covariance matrix. Since the original relationship between the states and the measurement in Eq. (5) is nonlinear, the estimation scheme can be iterated until convergence by successively replacing  $\bar{\mathbf{x}}$  by  $\hat{\mathbf{x}}$ , using the converged state estimate from the previous sampling time ( $t_{k-1}$ ) as the initial reference state  $\bar{\mathbf{x}}$ . The state estimate error covariance matrix  $\hat{\mathbf{P}}$  can then be computed from

$$\hat{\mathbf{P}} = (\mathbf{H}^T \mathbf{R}^{-1} \mathbf{H})^{-1} \quad (10)$$

Note that the aerodynamic state vector formulation is not unique. In particular, any two variables from the set of  $p_\infty$ ,  $p_t$ ,  $q_\infty$ ,  $R$ , and  $M_\infty$  can be used in the estimator in addition to  $\alpha$  and  $\beta$ . The remaining state variables not used directly in the estimator can be calculated as parameters, having first estimated the aerodynamic state variables. Note that the SEADS algorithm<sup>3</sup> made use of  $p_\infty$  and  $p_t$  in the estimator formulation.

Due to the asymptotic behavior of the pressure ratio as a function of Mach described in the previous section, some numerical difficulties can arise for high Mach number conditions. For high-Mach cases it may

be advantageous to consider a special case of estimators that use a fixed pressure ratio  $R$  and form state estimates using only three aerodynamic variables, e.g.  $p_t$ ,  $\alpha$ , and  $\beta$ , with dynamic pressure computed directly from  $p_t$  assuming the limiting value of the quantity  $RM_\infty^2$ . These estimators are generally more consistent but become biased as the true pressure ratio drifts away from the assumed value. If the vehicle is instrumented with an Inertial Measurement Unit (IMU) then it is also possible to schedule the assumed pressure ratio as a function of the inertial Mach number to reduce the growth of the bias over time. Alternately, the bias can be calibrated and subtracted out using preflight simulation cases.

The least-squares solution described in this section has several important properties. First, all pressure measurements are processed simultaneously to determine the atmospheric state variable estimate, opposed to the so-called “triples” algorithms, which use only a subset of available ports to determine the state variable estimates individually in sequence. Using all measurements simultaneously is advantageous in the sense that every port contributes to the state estimate rather than a restricted set, which generally leads to better performance,<sup>8</sup> and is also fault tolerant in the sense that a failed port can simply be removed from the solution that would otherwise ruin a triples algorithm.

### 1. Wind Estimation

Wind estimation is enabled by combining the MEADS algorithm outputs with velocity and attitude outputs derived from the IMU. One approach is to relate the angle of attack and sideslip estimates to the planet relative velocity and the horizontal wind components and solve directly for the winds using Newton’s method.<sup>9</sup> To this end, the aerodynamic angles can be expressed as

$$\tan \alpha = \frac{w_b}{u_b} \quad (11)$$

$$\tan \beta = \frac{v_b}{\sqrt{u_b^2 + v_b^2}} \quad (12)$$

where  $u_b$ ,  $v_b$  and  $w_b$  are the body-axis wind-relative velocities, which are in turn functions of the wind velocity and the planet-relative trajectory given by

$$\begin{Bmatrix} u_b \\ v_b \\ w_b \end{Bmatrix} = \mathbf{G}(\Psi, \Theta, \Phi) \begin{Bmatrix} u_g - u_w \\ v_g - v_w \\ w_g - w_w \end{Bmatrix} \quad (13)$$

where  $\Psi$ ,  $\Theta$ , and  $\Phi$  are the yaw-pitch-roll Euler angles relating the tangent frame to the body frame and  $\mathbf{G}$  is the matrix of the transformation,  $u_g$ ,  $v_g$  and  $w_g$  are the planet relative North-East-Down velocities, and  $u_w$ ,  $v_w$ , and  $w_w$  are the wind components.

At each air data measurement point occurring at time  $t_k$  with aerodynamic angle estimates given by  $\hat{\alpha}$  and  $\hat{\beta}$ , the wind velocities may be solved for by the iterative method (neglecting the downward wind)

$$\begin{Bmatrix} u_w \\ v_w \end{Bmatrix}_{j+1} = \begin{Bmatrix} u_w \\ v_w \end{Bmatrix}_j + \mathbf{\Gamma}^{-1} \begin{Bmatrix} \hat{\alpha} - \alpha(u_{w_j}, v_{w_j}) \\ \hat{\beta} - \beta(u_{w_j}, v_{w_j}) \end{Bmatrix} \quad (14)$$

where  $j$  is an iteration index, and

$$\mathbf{\Gamma} = \begin{bmatrix} \frac{\partial \alpha}{\partial u_w} & \frac{\partial \alpha}{\partial v_w} \\ \frac{\partial \beta}{\partial u_w} & \frac{\partial \beta}{\partial v_w} \end{bmatrix}_{(u_w=u_{w_j}, v_w=v_{w_j})} \quad (15)$$

The wind estimate error covariance matrix,  $\hat{\mathbf{P}}_w$ , follows from the measurement error covariance matrix,  $\hat{\mathbf{P}}$ , and from the planet-relative trajectory error covariance matrix,  $\hat{\mathbf{Q}}$ , by means of the equation

$$\hat{\mathbf{P}}_w = \mathbf{\Gamma}^{-1} \hat{\mathbf{P}} (\mathbf{\Gamma}^{-1})^T + \mathbf{\Lambda} \hat{\mathbf{Q}} \mathbf{\Lambda}^T \quad (16)$$

where

$$\mathbf{\Lambda} = \begin{bmatrix} \frac{\partial u_w}{\partial u_g} & \frac{\partial u_w}{\partial v_g} & \frac{\partial u_w}{\partial w_g} & \frac{\partial u_w}{\partial \psi} & \frac{\partial u_w}{\partial \theta} & \frac{\partial u_w}{\partial \phi} \\ \frac{\partial v_w}{\partial u_g} & \frac{\partial v_w}{\partial v_g} & \frac{\partial v_w}{\partial w_g} & \frac{\partial v_w}{\partial \psi} & \frac{\partial v_w}{\partial \theta} & \frac{\partial v_w}{\partial \phi} \end{bmatrix} \quad (17)$$

This method suffers from singularities in the matrix  $\Gamma$  when the flight path angle is zero.<sup>9</sup> This singular condition is problematic for the MEADS application since the MSL entry trajectory crosses zero flight path angle on two occasions, shown in Fig. 1(c).

## 2. Density Estimation

The freestream atmospheric density at time  $t_k$  follows the determination of the dynamic pressure and the wind-relative velocities from

$$\hat{\rho}_\infty = \frac{2\hat{q}_\infty}{(u_b^2 + v_b^2 + w_b^2)} \quad (18)$$

## B. Kalman Filter Formulation

The Kalman filter technique can be used to blend the MEADS and IMU measurements together in a tightly-coupled fashion, in order to compute the winds and atmospheric state variables directly from the MEADS measured surface pressures and integrated IMU accelerations and angular rates. The approach is to recast the pressure model to be written as a function of the freestream atmospheric quantities (pressure, density, and tangential winds) along with the planet-relative vehicle velocity and orientation. After computing these transformed states, the aerodynamic orientation angles, Mach number, and dynamic pressure are calculated as output parameters. A tightly-coupled solution of this nature has not been implemented before for entry vehicle trajectory reconstruction, though a conceptually similar philosophy has been proposed for real-time air data processing for aircraft applications in Ref. 10.

The proposed blended data processing technique for MEADS/IMU is modification to the Extended Kalman Filter (EKF) approach implemented in a trajectory reconstruction code known as *NewSTEP*. This code is a generalization of the Statistical Trajectory Estimation Program (STEP)<sup>11–13</sup> developed by NASA/LaRC and used extensively in the 1960s-1980s on a wide variety of launch vehicle and entry vehicle flight projects, including the X-23A/SV-5D PRIME,<sup>14</sup> Viking,<sup>15–17</sup> Pioneer Venus,<sup>18</sup> the Space Shuttle<sup>19,20</sup> and Titan IIIC.<sup>21</sup> The NewSTEP code borrows heavily from the STEP formulation, but includes several enhancements to the algorithms and implementation. In particular, NewSTEP is coded entirely in Matlab in order to make use of built-in capabilities such as numerical integration routines. The NewSTEP code has been applied to several projects including the Hyper-X Mach 7 and Mach 10 flights<sup>22</sup> and the Mars Exploration Rover (MER) mission. In addition to the MSL/MEDLI flight data processing, the code is planned to be used in support of the Inflatable Reentry Vehicle Experiment (IRVE and IRVE-II),<sup>23</sup> the Orion Launch Abort Flight Tests (PA-1), and the Ares I-X flight test.<sup>24</sup>

The NewSTEP code is designed to combine vehicle inertial data and external data sources over the entire time history in order to generate a state trajectory estimate and associated uncertainty estimates. The nonlinear filter dynamics are driven by acceleration and angular rate measurements from the on-board IMU. The NewSTEP code has been generalized for the MEADS data processing to incorporate tightly coupled pressure measurements to be included in the Kalman filter formulation. To do so, atmospheric state variables are included in the filter formulation such that the filter estimates the freestream atmospheric conditions (pressure, density, and winds) directly from the MEADS pressure measurements when combined with IMU data at each measurement update step. An iterative update has been added to NewSTEP in order to better capture the nonlinear relationship between the state variables and the measured pressures. Additionally, the option to include pressure transducer scale factor errors as “solve-for” parameters has been incorporated into the implementation.

The basic premise behind the proposed inertially blended atmospheric data filter is to reformulate the measured pressure model into one that directly incorporates planet-relative states and freestream atmospheric conditions. For example, in Newtonian flow theory the surface pressure distribution is usually written as a function of the angle of attack, angle of sideslip, dynamic (or total) pressure, and static pressure or the pressure ratio, e.g. Eq. (1). By substituting the relations Eqs. (11) and (12) and the relation for Mach number as the ratio of wind-relative velocity to the speed of sound, the surface pressure distribution can be written as a function of the planet-relative trajectory and freestream atmospheric conditions. This reformulation allows for a tight coupling between the IMU and the atmospheric data system in order to estimate the trajectory and atmosphere simultaneously.

The filter state variables used in this formulation are

$$\mathbf{x} = \begin{bmatrix} r & \theta & \phi & u & v & w & e_0 & e_1 & e_2 & e_3 & u_w & v_w & w_w & p_\infty & \rho_\infty \end{bmatrix}^T \quad (19)$$

where  $r$  is the radius of the vehicle from the center of the planet,  $\theta$  is the longitude,  $\phi$  is the declination,  $u, v, w$  are the inertial velocity components in a local-radial coordinate frame,  $e_i$  are the Euler parameters describing the attitude of the vehicle with respect to the local-vertical frame,  $u_w, v_w$  and  $w_w$  are the wind components in the local-vertical frame, and  $p_\infty$  and  $\rho_\infty$  are the freestream pressure and density, respectively.

The state dynamics are modelled with the nonlinear system of differential equations given by<sup>22</sup>

$$\dot{r} = -w \quad (20)$$

$$\dot{\phi} = \frac{u}{r} \quad (21)$$

$$\dot{\theta} = \frac{v}{r \cos \phi} - \Omega \quad (22)$$

$$\dot{u} = a_u + \frac{1}{r} (uw - v^2 \tan \phi) - \left( \frac{3\mu J_2}{2r^4} \right) \sin(2\phi) \quad (23)$$

$$\dot{v} = a_v + \frac{1}{r} (uv \tan \phi + vw) \quad (24)$$

$$\dot{w} = a_w - \frac{1}{r} (u^2 + v^2) + \frac{\mu}{r^2} - \left( \frac{3\mu J_2}{2r^4} \right) (2 - 3 \cos^2 \phi) \quad (25)$$

$$\begin{Bmatrix} \dot{e}_0 \\ \dot{e}_1 \\ \dot{e}_2 \\ \dot{e}_3 \end{Bmatrix} = \frac{1}{2} \begin{bmatrix} -e_1 & -e_2 & -e_3 \\ e_0 & -e_3 & e_2 \\ e_3 & e_0 & -e_1 \\ -e_2 & e_1 & e_0 \end{bmatrix} \left( \begin{Bmatrix} \omega_x \\ \omega_y \\ \omega_z \end{Bmatrix} - \frac{1}{r} \mathbf{G} \begin{Bmatrix} v \\ -u \\ -v \tan \phi \end{Bmatrix} \right) \quad (26)$$

$$\dot{p}_\infty = \frac{\rho_\infty w}{r^2} \quad (27)$$

$$\dot{\rho}_\infty = \frac{\rho_\infty^2 w}{r^2 p_\infty} \quad (28)$$

$$\dot{u}_w = 0 \quad (29)$$

$$\dot{v}_w = 0 \quad (30)$$

$$\dot{w}_w = 0 \quad (31)$$

where  $\mu$  is the gravitational parameter of the planet,  $J_2$  is the oblateness coefficient of the gravity field, and  $\Omega$  is the angular rate of the planet. The matrix  $\mathbf{G}$  is the transformation from the local-tangent frame to the body frame. The quantities  $\omega_x, \omega_y$  and  $\omega_z$  are the body-axis sensed angular rates, and  $a_u, a_v$  and  $a_w$  are body center of mass accelerations in the local frame, which are related to the sensed accelerations at the IMU location in the body frame via the equation,

$$\begin{Bmatrix} a_u \\ a_v \\ a_w \end{Bmatrix} = \mathbf{G}_r \left( \begin{Bmatrix} a_x \\ a_y \\ a_z \end{Bmatrix} - \begin{bmatrix} -(\omega_y^2 + \omega_z^2) & (\omega_x \omega_y - \dot{\omega}_z) & (\omega_x \omega_z + \dot{\omega}_y) \\ (\omega_x \omega_y + \dot{\omega}_z) & -(\omega_x^2 + \omega_z^2) & (\omega_y \omega_z - \dot{\omega}_x) \\ (\omega_x \omega_z - \dot{\omega}_y) & (\omega_y \omega_z + \dot{\omega}_x) & -(\omega_x^2 + \omega_y^2) \end{bmatrix} \begin{Bmatrix} x_m \\ y_m \\ z_m \end{Bmatrix} \right) \quad (32)$$

where  $a_x, a_y$ , and  $a_z$  are the sensed accelerations at the IMU location and  $x_m, y_m$ , and  $z_m$  are the IMU position coordinates in the body frame. Transducer scale factor errors can be included in the filter formulation using differential equations of the form  $\dot{\lambda}_i = 0$  where  $\lambda_i$  is the scale factor error of the  $i$ th transducer.

Additive process noise terms are included on the acceleration and angular rate measurements to account for sensor errors. Process noise terms are also included on the atmospheric winds, pressure, and density to account for model uncertainties.

Let the quantities  $\hat{\mathbf{x}}_{k-1}$  and  $\hat{\mathbf{P}}_{k-1}$  be the state estimate and state estimate error covariance at time step  $t_{k-1}$ , respectively, and let  $\bar{\mathbf{x}}_k$  and  $\bar{\mathbf{P}}_k$  be the predicted state and state error covariance at time  $t_k$ . The MEADS pressure measurement  $\mathbf{p}_k$  at time  $t_k$  is processed according to<sup>7</sup>

$$\hat{\mathbf{x}}_{k,i+1} = \bar{\mathbf{x}}_k + \mathbf{K}_{k,i} [\mathbf{p}_k - \mathbf{h}(\hat{\mathbf{x}}_{k,i}, t_k) - \mathbf{H}_{k,i} \cdot (\bar{\mathbf{x}}_k - \hat{\mathbf{x}}_{k,i})] \quad (33)$$

where  $i$  denotes the iteration index,  $\mathbf{h}(\mathbf{x}, t)$  is the predicted pressure measurement based on the surface pressure model and  $\mathbf{H}$  is its linearization about the current state estimate. The quantity  $\mathbf{K}_{k,i}$  is the Kalman gain matrix,

$$\mathbf{K}_{k,i} = \bar{\mathbf{P}}_k \mathbf{H}_{k,i}^T [\mathbf{H}_{k,i} \bar{\mathbf{P}}_k \mathbf{H}_{k,i}^T + \mathbf{R}_k]^{-1} \quad (34)$$

The filter equations above are iterated until convergence (or until reaching a prescribed upper limit on the number of iterations), leading to the final state estimate following the pressure measurement update. The estimated state covariance is then provided by

$$\hat{\mathbf{P}}_k = [\mathbf{I} - \mathbf{K}_k \mathbf{H}_k] \bar{\mathbf{P}}_k \quad (35)$$

where  $\mathbf{K}_k$  and  $\mathbf{H}_k$  are computed using the converged state estimate.

The state predictions from one measurement point to the next are computed using numerical integration of the nonlinear dynamic model in Eqs. (20–31). The covariance predictions are propagated according to the matrix differential equation

$$\dot{\bar{\mathbf{P}}}(t) = \mathbf{F}_x(\hat{\mathbf{x}}(t), t)\bar{\mathbf{P}}(t) + \bar{\mathbf{P}}(t)^T \mathbf{F}_x(\hat{\mathbf{x}}(t), t)^T + \mathbf{F}_u(\hat{\mathbf{x}}(t), t)\mathbf{Q}(t)\mathbf{F}_u(\hat{\mathbf{x}}(t), t)^T \quad (36)$$

$$\bar{\mathbf{P}}(t_{k-1}) = \hat{\mathbf{P}}_{k-1} \quad (37)$$

where  $\mathbf{F}_x$  and  $\mathbf{F}_u$  are the linearizations of the system dynamics with respect to the states and process noise terms, respectively, and  $\mathbf{Q}$  is the process noise covariance matrix.

## IV. System Performance

The impact of individual error sources and the effects of selected failure modes are examined in this section. These error sources include port location knowledge, sensor noise and quantization, telemetry time stamp errors, pneumatic lag, thermal transpiration, and system calibration uncertainties. The associated error models are reviewed in the following sections before showing sensitivity simulation results. The CFD pressure distributions uncertainties are not considered in this work.

### A. Error Models

#### 1. Port Location Knowledge Error

Errors in the knowledge of the port location after installation are cast as random longitudinal perturbations at constant clock angle and a random tangential perturbation at constant cone angle. The errors are specified as uncorrelated zero-mean Gaussian random numbers. The measurement system is accurate to within 0.05 inches in a  $3\sigma$  sense.

#### 2. Noise and Quantization

Sensor noise is modeled using the equation

$$\hat{P}_i = P_i + (P_{max} - P_{min}) \eta_p \quad (38)$$

where  $P_i$  is the transducer output, and  $P_{max}$  and  $P_{min}$  are the maximum and minimum pressure range of the sensor system, respectively. The variable  $\eta_p$  is a uniform random variable between  $\pm N/2^n$  where  $N$  is the number of counts of noise and  $n$  is the system effective bit size.

Sensor quantization can be modelled using the equation

$$\tilde{P}_i = \left( \frac{P_{max} - P_{min}}{2^n} \right) \text{Int} \left[ \left( \frac{\hat{P}_i}{P_{max} - P_{min}} \right) 2^n \right] \quad (39)$$

Finally, sensor saturation can be modeled as  $\bar{P}_i = \max \left[ \min \left( \tilde{P}_i, P_{min} \right), P_{max} \right]$ .

#### 3. Timing Error

Relative errors in the telemetry time stamp between measurements at different port locations introduces a distortion effect that corrupts the pressures used as input to the basic data reduction algorithm. Timing errors include both random and systematic components. The systematic timing errors can be adjusted in pre-processing of the flight data, leaving only the random error to be considered in error budgeting. These errors are simulated by first casting a uniform random number for each port in the range of  $\pm 25\mu s$ , and then shifting the truth state used to calculate the measured surface pressures.

#### 4. Pneumatic Lag

The MEADS system response model, or lag model, captures the dynamics of the pressure measurement from the surface port location to the pressure transducer (the sensor). In general, these characteristics are a function of the line properties (tube diameter and length), fluid properties (density, dynamic viscosity, etc.), as well as flight conditions (pressure and temperature at the port and temperature at the transducer). The system response models are used to accomplish two objectives: firstly, to accurately model the response so that pre-flight simulation can be used to assess hardware, algorithms, and telemetry rates, and secondly, to characterize the system response so that measured pressures can be corrected to actual surface pressures for use in generating atmospheric data estimates.

High-fidelity response models based on the Navier–Stokes equations are available in the literature, in particular the infinite-order frequency-domain Bergh–Tijdeman response model<sup>25</sup> and variations on this model for branched systems developed by Whitmore.<sup>26</sup> In these models, the pneumatic system is broken up into a series of segments, each with constant line and fluid properties. The end to end frequency response from port to transducer becomes the product of the individual response functions for each segment. Entrapped volume in any of the segments can also be captured. In this manner changes in tubing diameter as well as temperature gradients can be explicitly modelled. The response is evaluated across a range of input frequencies and the result is a complex frequency response that can be represented as magnitude and phase.

The frequency domain results for each flight condition are not readily suited either for time domain simulation or for direct analysis of time histories of measured pressure. For these purposes, a low-order response model must be utilized. For simple 2nd order systems, this response can be characterized by a natural frequency and damping, with transfer functions of the form

$$\frac{P_L}{P_0} = \frac{\omega_n^2}{s^2 + 2\zeta\omega_n + \omega_n^2} \quad (40)$$

where  $P_0$  is the applied pressure,  $P_L$  is the lagged pressure, and  $\zeta$  and  $\omega_n$  are the damping ratio and natural frequency, respectively, and  $s$  is the Laplace variable.

A variety of 2nd order models based on simplified fluid mechanics relations are available in the literature with varying assumptions and classifications.<sup>27</sup> A new 2nd order response model based on first principles is presented in Ref. 27. This model is derived directly from the Bergh–Tijdeman equations using order reduction techniques and was found to be more accurate than other 2nd order models. The natural frequency and damping coefficients of this model are

$$\omega_n^2 = \frac{A_c c^2 / LV}{(LA_c/2V) \left[ 1 + (1/12) (\gamma L R_d)^2 / (c \rho_0)^2 \right] + 1 + (1/6) (\gamma L R_d)^2 / (c \rho_0)^2} \quad (41)$$

$$\zeta = \frac{\omega_n}{2} \left( \frac{\gamma R_d}{\rho_0} \right) \left[ \frac{VL}{A_c c^2} + \frac{1}{2} \left( \frac{L}{c} \right)^2 \right] \quad (42)$$

where  $L$  is the tube length,  $A_c$  is the cross-sectional area,  $V$  is the transducer entrapped volume,  $\rho_0$  is the fluid density in the tube,  $c$  is the speed of sound, and  $\gamma$  is the ratio of specific heats. The parameter  $R_d$  is known as the acoustic impedance and can be calculated as a function of Reynold's number to capture laminar, transitional, or turbulent flow conditions, as described in Ref. 27.

Another approach to time domain analysis is look for a low-order system that matches the model response. This assumed form of this equivalent system is chosen to capture the modelled dynamics and to facilitate efficient simulation. Numerical optimization techniques have been utilized to fit transfer function models to the high-fidelity frequency response model, including up to 4th order systems with pure time delay. Preliminary results of this approach have been documented in Refs. 28 and 29 but will not be discussed in this paper.

#### 5. Thermal Transpiration

Under rarefied flow conditions, transpiration induced effects within a tubing system can cause the pressure measured by the transducers to be significantly different from the surface pressure. The effects can be divided into those caused by temperature gradients between the transducer and the surface, and those caused by heat transfer and/or shear stress.

A study of the available literature yielded three models to account for transpiration effects; two models for simulating the difference between measured and orifice pressure due to thermomolecular flow effects and one

model for simulating the difference between the surface and orifice pressure due to shear stress and/or heat transfer. The first transpiration model is provided in Ref. 30, which is an application of thermomolecular flow theory developed by Knudsen in Ref. 32. Knudsen's general formula for the thermomolecular pressure effect is

$$\frac{dP}{dT} = \frac{1}{(1 + a'r/\lambda)^2} \frac{P}{2T}, \quad \text{where } a' = a_1 \frac{1 + a_2 r/\lambda}{1 + a_3 r/\lambda} \quad (43)$$

where  $r$  is a physical length scale,  $\lambda$  is the mean free path,  $P$  is the pressure,  $T$  is the temperature, and  $a_1$ ,  $a_2$ , and  $a_3$  are empirical constants. The empirical constants have been obtained by Knudsen, using least-squares fit to data acquired with hydrogen in glass tubes.<sup>32</sup> The results are  $a_1 = 2.46$ ,  $a_2 = 3.15$ , and  $a_3 = 24.6$ .

Assuming that the temperature in the tubing between the surface and the transducer is known as a function of length  $x$ , Eq. (43) can be written as

$$\frac{\partial P(x)}{\partial x} = \frac{P(x)}{2T(x)} \left[ \frac{\partial T(x)}{\partial x} \right] \left[ \frac{\kappa(P, T, D)^2 + a_1 \kappa(P, T, D)}{\kappa(P, T, R)^2 + (a_1 + a_2) \kappa(P, T, D) + a_2 a_3} \right]^2 \quad (44)$$

where the parameter  $\kappa$  is the Knudsen number, given by

$$\kappa = \frac{\mu}{DP} \sqrt{\frac{\pi R_g T}{2}} \quad (45)$$

where  $R_g$  is the specific gas constant. The viscosity  $\mu$  can be calculated as a function of temperature using Sutherland's relation<sup>33</sup>

$$\mu = \mu_0 \left( \frac{T_0 + C}{T + C} \right) \left( \frac{T}{T_0} \right)^{3/2} \quad (46)$$

The constants associated with carbon dioxide are summarized in Table 1.

**Table 1. Gas Constants for Carbon Dioxide**

Constant	Value
$R_g$ , J/kg-K	191.8
$\mu_0$ , Pa-s	$14.8 \cdot 10^{-6}$
$T_0$ , K	293.15
$C$ , K	240.0

The second transpiration model is based on an algorithm described by Potter.<sup>34</sup> This model is based on the theoretical formulation of Ref. 35 and empirical data obtained in Ref. 36. The empirical data were obtained in a sequence of experiments involving a wide range of tube lengths, diameters, orifice shapes, and gases, including hydrogen, helium, nitrogen, and argon. The model is

$$\frac{\partial P(x)}{\partial x} = \frac{P(x)}{2T(x)} \left[ \frac{\partial T(x)}{\partial x} \right] \left[ 1 + \frac{b_1}{\kappa(P, T, D)} + \frac{b_2}{\kappa(P, T, D) + b_3/\kappa(P, T, D)} \right]^{-2} \quad (47)$$

where  $b_1 = 0.275$ ,  $b_2 = 0.625$ , and  $b_3 = 24.0$ .

Note that both the Knudsen and Potter transpiration models predict that  $(\partial P/\partial x) \rightarrow 0$  as  $\kappa \rightarrow 0$ .

The last model investigated for this paper is an augmentation of the Potter model<sup>34</sup> that includes non-equilibrium effects due to heat transfer and shear stress. This model is described in Ref. 37. The solution relies on empirical fits to data obtained in a wide range of experiments. The algorithm for calculating non-equilibrium effects is complicated and is not repeated here.

## 6. System Calibration and Temperature Uncertainty

A calibration of the MEADS flight system was conducted in order to compute pressure as a function of Voltage and sensor/electronics temperature. The MEADS calibration program carried two independent calibration efforts. The baseline approach involved the industry standard or “traditional” method, successfully employed on SEADS<sup>38–40</sup> and Aeroassist Flight Experiment (AFE)<sup>41</sup> programs. The second approach is a proof-of-concept experiment using a Design of Experiments (DOE) method, which has never been used to calibrate

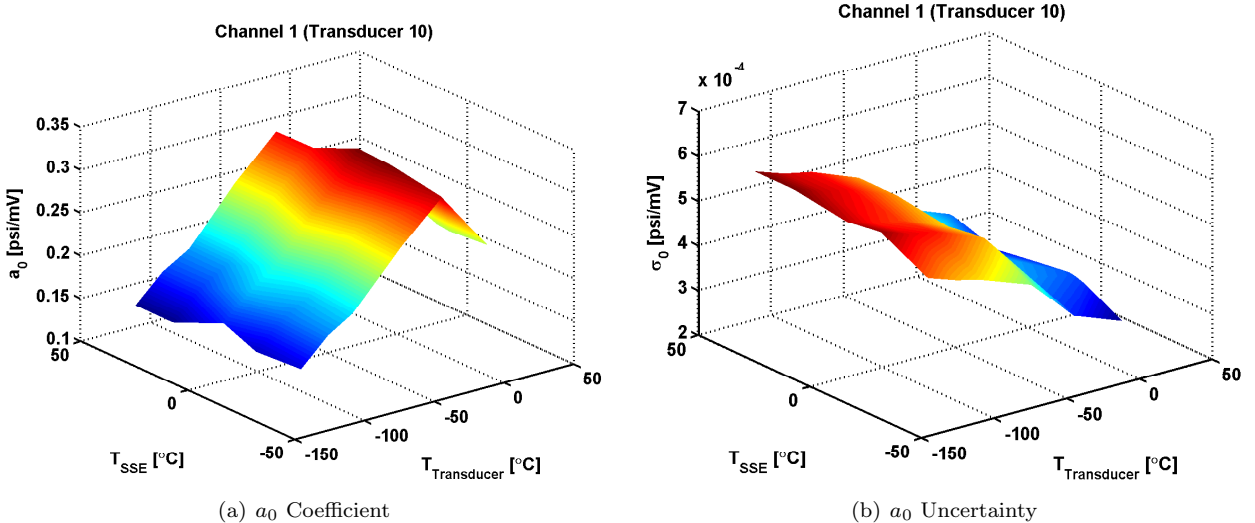


**Figure 5. Calibration Database Example**

space flight transducers prior to MEADS. The DOE approach is documented in Ref. 42 and is not discussed further in this paper.

The traditional calibration method uses a least-squares fit for each transducer to a model of the form

$$p = a_0(T_1, T_2) + a_1(T_1, T_2)V + a_2(T_1, T_2)V^2 \quad (48)$$

where  $T_1$  is the pressure head temperature,  $T_2$  is the SSE electronics temperature,  $V$  is the Voltage output from the transducer, and  $p$  is the pressure. The coefficients  $a_0$ ,  $a_1$ , and  $a_2$  are termed the bias, sensitivity, and nonlinearity, respectively. These coefficients are determined from a least-squares fit of pressure vs. Voltage at specific temperature set points using a simple increasing/decreasing applied pressure to create the voltage response. By varying the temperature set points, a database of calibration coefficients can be constructed, and an empirical model developed that uses spline interpolation to look up values of these coefficients as functions of the two temperatures.

Along with the values of the calibration coefficient, the uncertainties in the coefficients are also stored as a function of the two temperatures. These uncertainties can be used to build a calibration error model to assess system performance. The uncertainty analysis must also consider the effects of the in-flight zero, in which the bias is effectively removed from the model by taking a measurement in space shortly before atmospheric entry. A small residual bias error remains due to the slope of the bias curve as a function of temperature, coupled with temperature uncertainty and noise.

Let  $T_1^*$  and  $T_2^*$  be the transducer and SSE temperatures and  $V^*$  be the measured voltage at the time of the in-flight zero prior to atmospheric entry. Then the pressure error is

$$\delta p = a_0(T_1^*, T_2^*) + a_1(T_1^*, T_2^*)V^* + a_2(T_1^*, T_2^*)(V^*)^2 \quad (49)$$

Then the adjusted pressure is given by  $\hat{p} = p - \delta p$ . Following this correction, the estimated pressure is reset to read zero output at zero applied pressure. However, residual bias error remains due to the gradient of the  $a_0$  coefficient in the presence of temperature uncertainty. The in-flight zero does nothing to aid the knowledge of the transducer sensitivity and nonlinearity.

Let the measured transducer temperature be given by  $\hat{T}_1 = T_1 + b_1 + n_1$  where  $T_1$  is the true temperature,  $b_1$  is the bias error, and  $n_1$  is a noise component. Similarly let the measured SSE temperature be given by  $\hat{T}_2 = T_2 + b_2 + n_2$ . The uncertainty in the estimated pressure due to calibration uncertainty and temperature uncertainty can be derived by first expanding the equation for the adjusted pressure measurement as

$$\hat{p} = a_0(\hat{T}_1, \hat{T}_2) + a_1(\hat{T}_1, \hat{T}_2)V + a_2(\hat{T}_1, \hat{T}_2)V^2 - a_0(\hat{T}_1^*, \hat{T}_2^*) - a_1(\hat{T}_1^*, \hat{T}_2^*)V^* - a_2(\hat{T}_1^*, \hat{T}_2^*)(V^*)^2 \quad (50)$$

For purposes of uncertainty analysis, the Voltage  $V^*$  can be assumed to be zero. Thermal analysis of the MSL vehicle has shown a nearly constant temperature from the time of the in-flight zero throughout the atmospheric entry, though the initial temperature can vary widely.<sup>42</sup> Therefore the temperatures at the

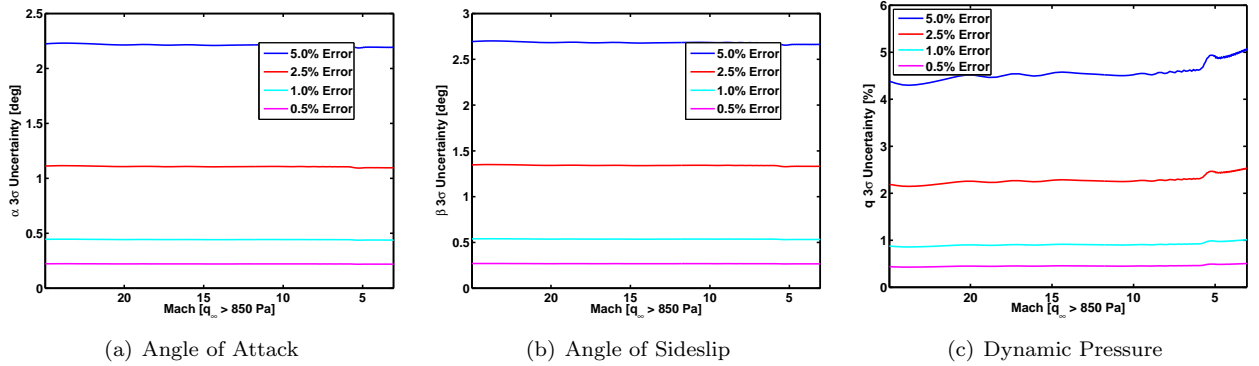


**Figure 6. Total System Performance Trade Study**

in-flight zero condition can be written as  $\hat{T}_1^* = T_1 + b_1 + n_1^*$  and  $\hat{T}_2^* = T_2 + b_2 + n_2^*$ , where  $n_1^*$  and  $n_2^*$  are the noise samples at the in-flight zero. Substituting these expressions into Eq.(50) and linearizing for small temperature errors leads to an expression for the pressure calibration error of the form

$$\begin{aligned} \sigma_p^2 &= 2\sigma_n^2 \left[ \left( \frac{\partial a_0}{\partial T_1} \right)^2 + \left( \frac{\partial a_0}{\partial T_2} \right)^2 \right] + \left[ \sigma_{a_1}^2 + \left( \frac{\partial a_1}{\partial T_1} \right)^2 (\sigma_n^2 + \sigma_b^2) + \left( \frac{\partial a_1}{\partial T_2} \right)^2 (\sigma_n^2 + \sigma_b^2) \right] V^2 \\ &\quad + \left[ \sigma_{a_2}^2 + \left( \frac{\partial a_2}{\partial T_1} \right)^2 (\sigma_n^2 + \sigma_b^2) + \left( \frac{\partial a_2}{\partial T_2} \right)^2 (\sigma_n^2 + \sigma_b^2) \right] V^4 \end{aligned} \quad (51)$$

where  $\sigma_n$ ,  $\sigma_b$ ,  $\sigma_{a_1}$  and  $\sigma_{a_2}$  are the thermocouple noise, thermocouple bias, slope, and nonlinearity standard deviations, respectively. Note that the bias uncertainty is removed through the in-flight zero, however a residual bias error remains due to the slope of the bias curve as a function of temperature, coupled with temperature uncertainty due to noise.

## 7. IMU Error Model

An inertial measurement unit (IMU) error model is required for the analysis of the wind estimation techniques using either the loosely coupled least-squares approach or the tightly-coupled Kalman filtering approach described in Sec. III. The loosely coupled least-squares solution requires a navigation error model as well, whereas the tightly coupled approach integrates the IMU measurements itself so that the navigation errors are captured in the state estimate error covariance matrix. The IMU measurement error and linear navigation error model implemented for the least-squares uncertainty analysis is based on the error analysis presented in Ref. 44. The IMU measurement error model for the Kalman filtering approach is described in Ref. 22. In both cases, systematic error parameters and noise uncertainty inputs to the models are described in Ref. 45.

## B. Error Analysis Results

This section describes error analysis results and test cases in order to assess system performance and sensitivities.

### 1. Total System Performance

The basic MEADS least-squares algorithm was used in a performance trade study in order to determine the total system accuracy requirements based on the science objectives of 0.5 deg angle of attack and sideslip, 2% dynamic pressure, and 0.1 Mach number uncertainties. A series of Monte-Carlo simulation studies were conducted with random multiplicative pressure error levels of 0.5%, 1.0%, 2.5% and 5.0% of reading. These Monte-Carlo simulations were conducted using 3000 runs with a Newtonian flow pressure model and the least-squares estimator formulated using a fixed pressure ratio of  $R = 0.001$ . The results of this study are shown in Fig. 6. From these plots it can be determined that a total system error of 1% of reading meets the science objectives on the angle of attack, sideslip, and dynamic pressure error levels. Therefore, total system error levels of 1% of reading became the requirements for system design.

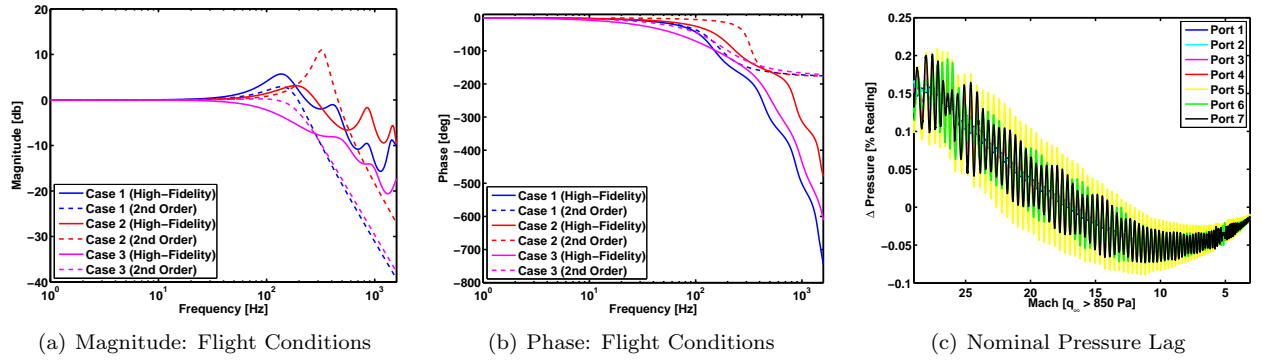


**Figure 7. Tube Response**

## 2. Pneumatic Lag Sensitivity

Due to computational complexities of simulating the tube and transducer response, these models were employed in a stand-alone manner in order to assess impacts to system performance. These studies include both the high-fidelity frequency domain models suitable for analyzing specific flight conditions as well as 2nd-order approximate models suitable for analyzing time histories.

The first study is an assessment of the port diameter. Three flight conditions were explored using the high-fidelity frequency response model, including a high Mach/low pressure case, the maximum pressure case, and a low Mach/low pressure case. The frequency response for these three conditions are shown in Fig. 7(a) and (b). The frequency response of the 2nd order model is also shown for comparison. Table 2 shows several important metrics of the frequency response for these three flight conditions. Here, the time constant and the time delay (computed from phase loss at 1 Hz frequency) are shown corresponding to the high-fidelity (HF) model as well as the 2nd order model. While differences are apparent between the HF and 2nd order models, the trends and orders of magnitude are similar. These results agree to within a factor of 2 or better with an independent implementation using a reduced-order Bergh-Tijdeman model described in Ref. 46. These results indicate that the response time is acceptable even for the worst-case lag time at the low Mach, low pressure condition.

**Table 2. Response Model Conditions and Results**

Condition	$M_\infty$	$q_\infty$ , Pa	$P$ , Pa	$\tau$ , sec (HF)	$\tau$ , sec (2nd)	$\Delta t$ , sec (HF)	$\Delta t$ , sec (2nd)
1 (High Mach)	29.0	850.0	1630.0	$0.34 \cdot 10^{-3}$	$0.72 \cdot 10^{-3}$	$0.70 \cdot 10^{-3}$	$0.75 \cdot 10^{-3}$
2 (Max $q_\infty$ )	16.8	14015.3	26788.5	$0.45 \cdot 10^{-3}$	$0.33 \cdot 10^{-3}$	$0.55 \cdot 10^{-3}$	$0.14 \cdot 10^{-3}$
3 (Low Mach)	3.1	850.0	1595.7	$1.31 \cdot 10^{-3}$	$0.78 \cdot 10^{-3}$	$2.01 \cdot 10^{-3}$	$1.09 \cdot 10^{-3}$

A time history of the pressure difference computed using the 2nd order model is shown in Fig. 7(c). If the input signal is of sufficiently low frequency content, then these lag effects can be corrected by inverting the transfer function to solve for the pressure signal at the port. Errors in the corrected pressure response are a combination of input uncertainties to the model and inherent error in the modelled physics. The effects of geometric uncertainties in the tube length and diameter are investigated in this section. Establishing bounds on the physics uncertainties is not discussed in this paper.

**Table 3. Response Model Port Diameter Results**

Port Diameter, in	$\tau$ , sec (HF)	$\tau$ , sec (2nd)	$\Delta t$ , sec (HF)	$\Delta t$ , sec (2nd)
0.07	$6.13 \cdot 10^{-3}$	$0.86 \cdot 10^{-3}$	$6.61 \cdot 10^{-3}$	$1.21 \cdot 10^{-3}$
0.04	$5.69 \cdot 10^{-2}$	$0.96 \cdot 10^{-3}$	$5.49 \cdot 10^{-2}$	$1.36 \cdot 10^{-3}$
0.02	2.62	$1.04 \cdot 10^{-3}$	0.22	$1.47 \cdot 10^{-3}$

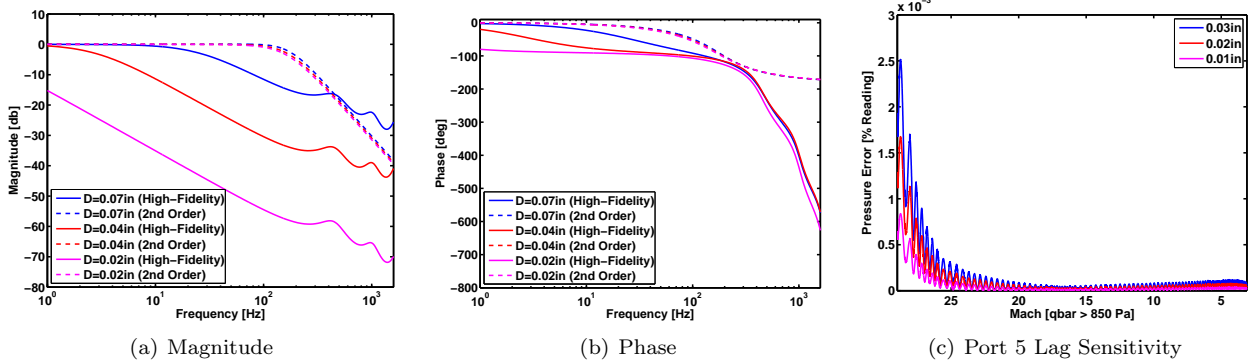


Figure 8. Tube Response: Diameter Sensitivity

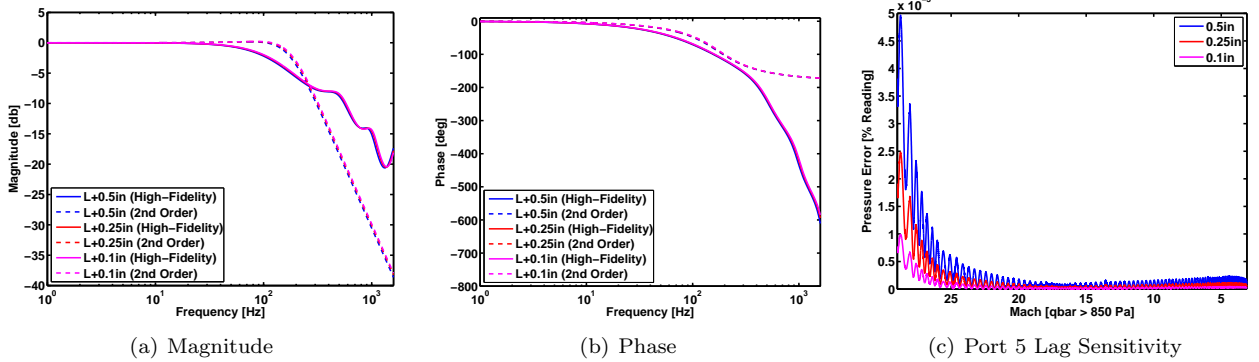


Figure 9. Tube Response: Length Sensitivity

Table 3 shows the results of a study varying the port diameter for the worst-case flight condition (low pressure, low Mach) discussed above. Here, the port diameter is varied to as low as 0.02in. These results indicate that the 0.07in case may be acceptable but the 0.04in case and below quickly become unacceptable. Figures 8(a) and (b) show the frequency response of the high-fidelity and 2nd-order models for these port diameters. Discrepancies between the HF and 2nd order models tend to increase with decreasing port diameter. Arc jet tests conducted for various port diameters indicate that the 0.10in case is acceptable,<sup>47</sup> therefore the diameter has been kept as originally designed. However, these results serve to indicate the sensitivity to the port diameter, therefore the diameter uncertainties should be kept as small as possible. Currently, the diameter uncertainty requirement on the tube system is 0.01in.<sup>2</sup> The port 5 (worst-case port) pressure lag error due to diameter uncertainty is shown in Fig. 8(c) for a range of diameter uncertainty up to 0.03in. In all cases the lag error is small (note that the errors are shown in % of reading).

Table 4. Response Model Tube Length Results

Tube Length, in	$\tau$ , sec (HF)	$\tau$ , sec (2nd)	$\Delta t$ , sec (HF)	$\Delta t$ , sec (2nd)
+0.1	$1.22 \cdot 10^{-3}$	$0.80 \cdot 10^{-3}$	$2.03 \cdot 10^{-3}$	$1.11 \cdot 10^{-3}$
+0.25	$1.26 \cdot 10^{-3}$	$0.82 \cdot 10^{-3}$	$2.08 \cdot 10^{-3}$	$1.14 \cdot 10^{-3}$
+0.5	$1.31 \cdot 10^{-3}$	$0.84 \cdot 10^{-3}$	$2.15 \cdot 10^{-3}$	$1.18 \cdot 10^{-3}$

Next, a study was conducted to assess the sensitivity to tube length. Three cases were investigated using at the low pressure, low Mach flight condition. Table 4 summarizes the effects perturbing the total tube length by increments of 0.1in, 0.25in, and 0.5in. In each case the time constant and time delay metrics do not change considerably. Figures 9(a) and (b) show the frequency response results for these perturbations. These results indicate that the pressure system is not highly sensitive to the tube length. Currently, the MEADS requirement on tube length uncertainty is 0.1in.<sup>2</sup> Figure 9(c) shows the time history of the lag error

for port 5 induced by length uncertainties of up to 0.5in. As in the previous case, these errors are acceptably small.

### 3. Thermal Transpiration Sensitivity

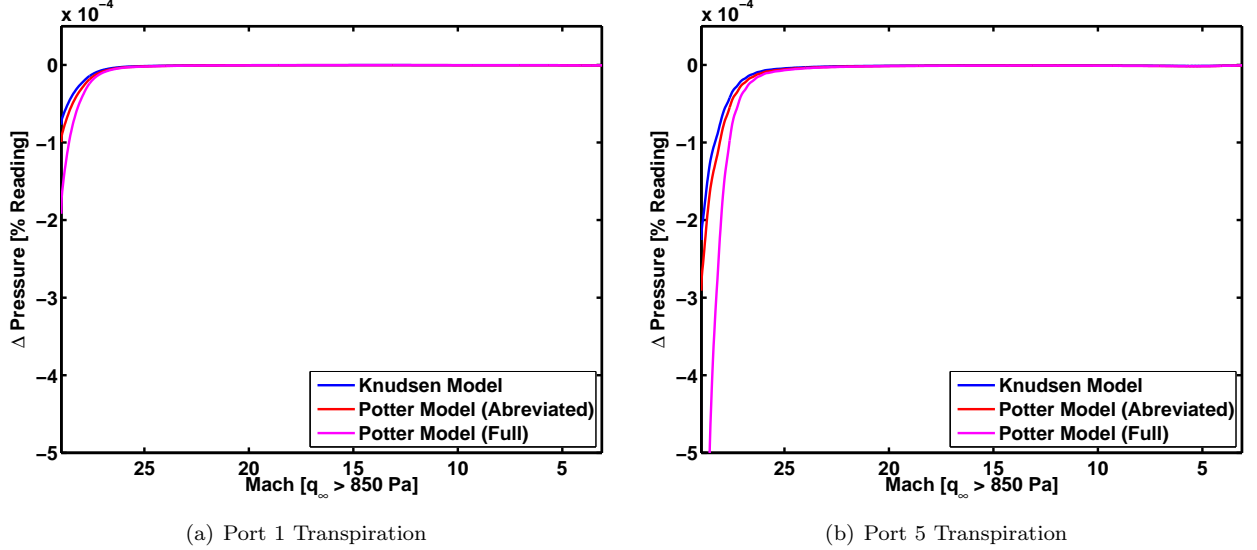


**Figure 10. Thermal Transpiration Results**

The thermal transpiration models were employed in stand-alone codes in order to assess impacts to system performance. Figure 10 shows the results of an analysis comparing the thermal transpiration models along the nominal reference trajectory. Here, the pressure difference between the nominal pressure and the pressure with the thermal transpiration effects is shown for Ports 1 and 5. Results are shown for the Knudsen model, the abbreviated Potter model (i.e. without orifice effects) and the full Potter model including the orifice effects. While some difference are apparent between the Knudsen and Potter models, all show the same trend with similar magnitudes. These results indicate that above 850 Pa dynamic pressure, the thermal transpiration effects are negligible.

### 4. System Performance Results

This section describes a system performance analysis on the MEADS algorithms. The error sources included in this study are the port location uncertainties, time tag errors, and system calibration uncertainties including temperature uncertainties. Pneumatic lag models and thermal transpiration effects are not considered in this study, as these errors are expected to be small. IMU and navigation errors are included for determining wind estimation uncertainties. Performance analysis results are shown for several estimator formulations. First, least-squares estimators have been implemented that use the dynamic pressure and either the Mach number or static pressure as solution variables, in addition to the angle of attack and sideslip. Additionally, results for a multi-pass Kalman filter approach are shown. In this approach, the first pass through the data estimates the pressure transducer scale factor errors in addition to the inertial and atmospheric state. Then, the pressure measurements are corrected using the computed scale factor errors, which reduces the total system uncertainty. The second pass through the data uses this corrected data set to estimate the inertial and atmospheric states. Each estimator uses the CFD database as the surface pressure distribution model. The least-squares estimators are assessed using a 500 case Monte-Carlo simulation, whereas the Kalman filter performance is simulated using a linear covariance analysis. Figure 11(a) shows the total system uncertainty used in these simulations. Figure 11(b) shows the system uncertainties after the scale factor correction from the Kalman filter. The MEADS primary science objectives are shown in Fig. 12. These plots show the  $3\sigma$  performance of the angle of attack, angle of sideslip, dynamic pressure, and Mach number estimates from the two least-squares formulations and both passes from the Kalman filter. The least-squares solutions are almost identical in these cases, and an improvement is apparent between the first and second pass of the Kalman filter solution. These results indicate that the MEADS-only angle of attack objectives are met through a large portion of the trajectory but begin to grow above the goal of 0.5 deg accuracy in the low

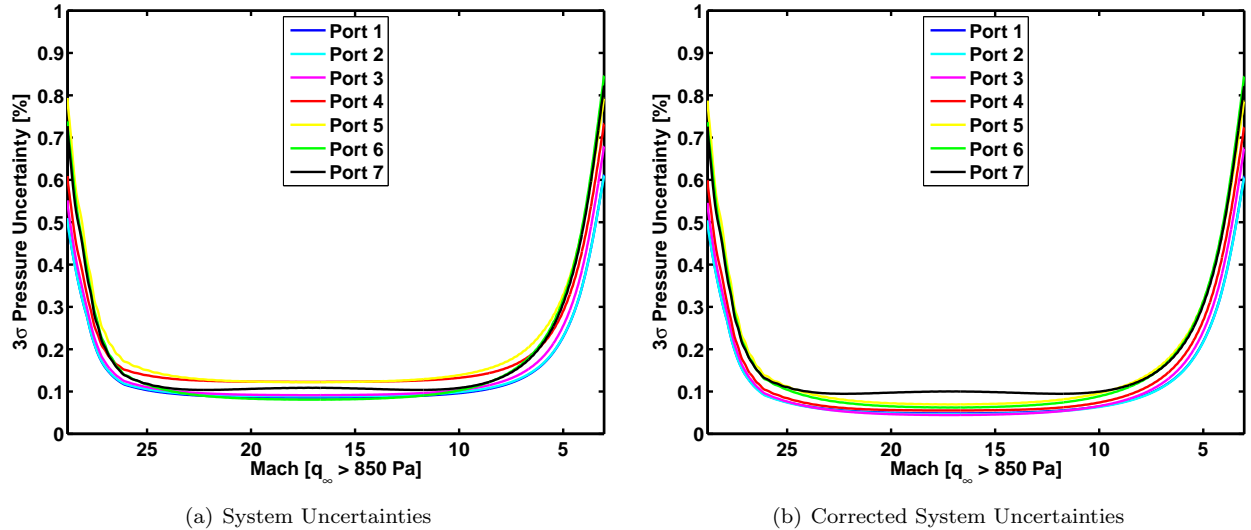


**Figure 11. Pressure System Uncertainties**

Mach regime. The same is true of the sideslip results although the growth above 0.5 deg is smaller than that of the angle of attack. The dynamic pressure objectives are met easily in these cases, however the Mach number estimates are not met throughout the trajectory. The Mach number results follow basic intuition that the Mach number is not observable in the high Mach regimes.

The  $3\sigma$  accuracies of the MEADS secondary objectives are shown in Fig. 13. Specifically, these plots show the static pressure, density, total pressure, and wind estimate performance. The static pressure results shows differences between the two least-squares solutions. In the high Mach regime, the estimator formulation using the static pressure as a solution variable exhibits a higher error than that using the Mach number. This behavior is likely due to the small pressure ratio combined with small static pressure at these conditions. Later on, as the static pressure and pressure ratio increases as the Mach number decreases, the observability on the static pressure is better, leading to better estimates when including static pressure in the solution set. Given that these estimators perform so differently on estimating the static pressure but the dynamic pressure estimates are essentially identical is in keeping with the observations made in Sec. II that the dynamic pressure can be computed accurately even in the presence of large static pressure uncertainties.

The wind estimates from the loosely-coupled IMU/least-squares formulations are poor in the flight regions shown here. This behavior is due to the nearly zero flight path angle in these flight regimes, rendering the wind estimator nearly singular. In regions below 850 Pa dynamic pressure in the low Mach regime, the flight path angle is increasing in magnitude, which has the effect of improving the wind estimate performance. The density estimates of the loosely-coupled formulation are also poor due to the large errors in the wind estimates. The tightly-coupled Kalman filter formulations are significantly superior in estimating the atmospheric winds and densities, and moreover can estimate the downward wind component.

## V. Current Status and Future Work

Although the pressure transducers passed acceptance testing, a variety of workmanship issues were uncovered in the course of conducting the thermal calibration and environmental testing. One transducer failed completely and all others were disqualified from flight status. New transducers are being manufactured by the vendor, with increased cleanliness and workmanship oversight from NASA. These will be delivered in the late summer of 2009. Receipt inspection and preliminary thermal characterization will take place at NASA-LaRC, and assignments of Flight and Flight Spare will be made. Environmental acceptance testing will take place at LaRC in the Fall of 2009, with delivery and integration with MSL in early CY 2010. Preliminary plans are also being made for the acceptance and processing of the flight data following Mars entry in 2012.

Several potential areas with regard to estimator performance and error modelling can be investigated. Investigations will be performed to assess estimator performance in regions below dynamic pressure of 850 Pa. In these regions, especially in the high Mach/high altitude regime, the tube response modelling and thermal

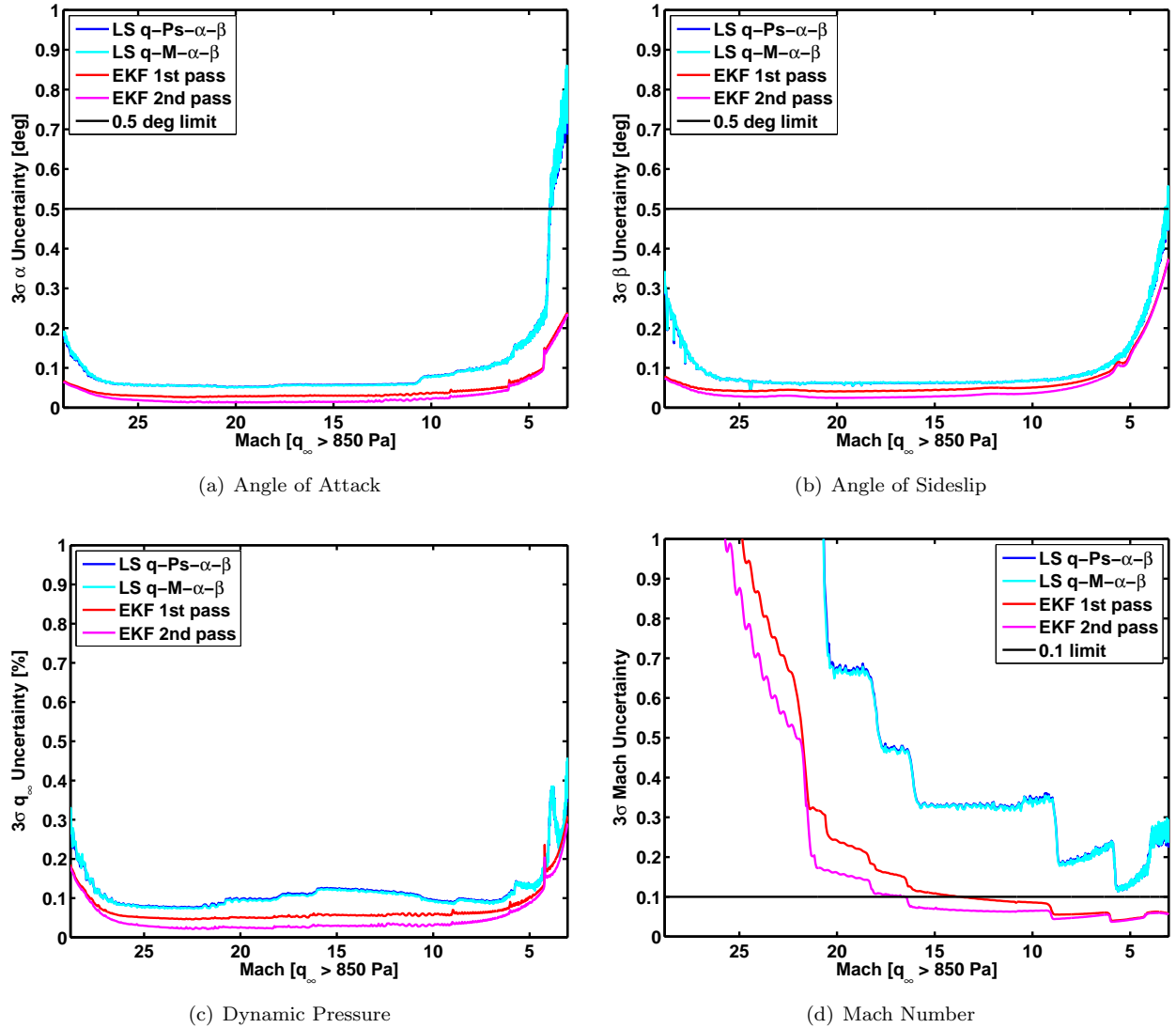


Figure 12. MEADS Primary Science Objectives

transpiration effects become much more pronounced and therefore an understanding of model uncertainties needs to be established in order to develop realistic estimator performance results. To this end, a series of shock tube tests are planned to investigate response model uncertainties. Investigations can be conducted to determine the feasibility of incorporating the MISP stagnation thermocouple measurements into the Kalman filter solution, which may give additional observability on the freestream Mach number.

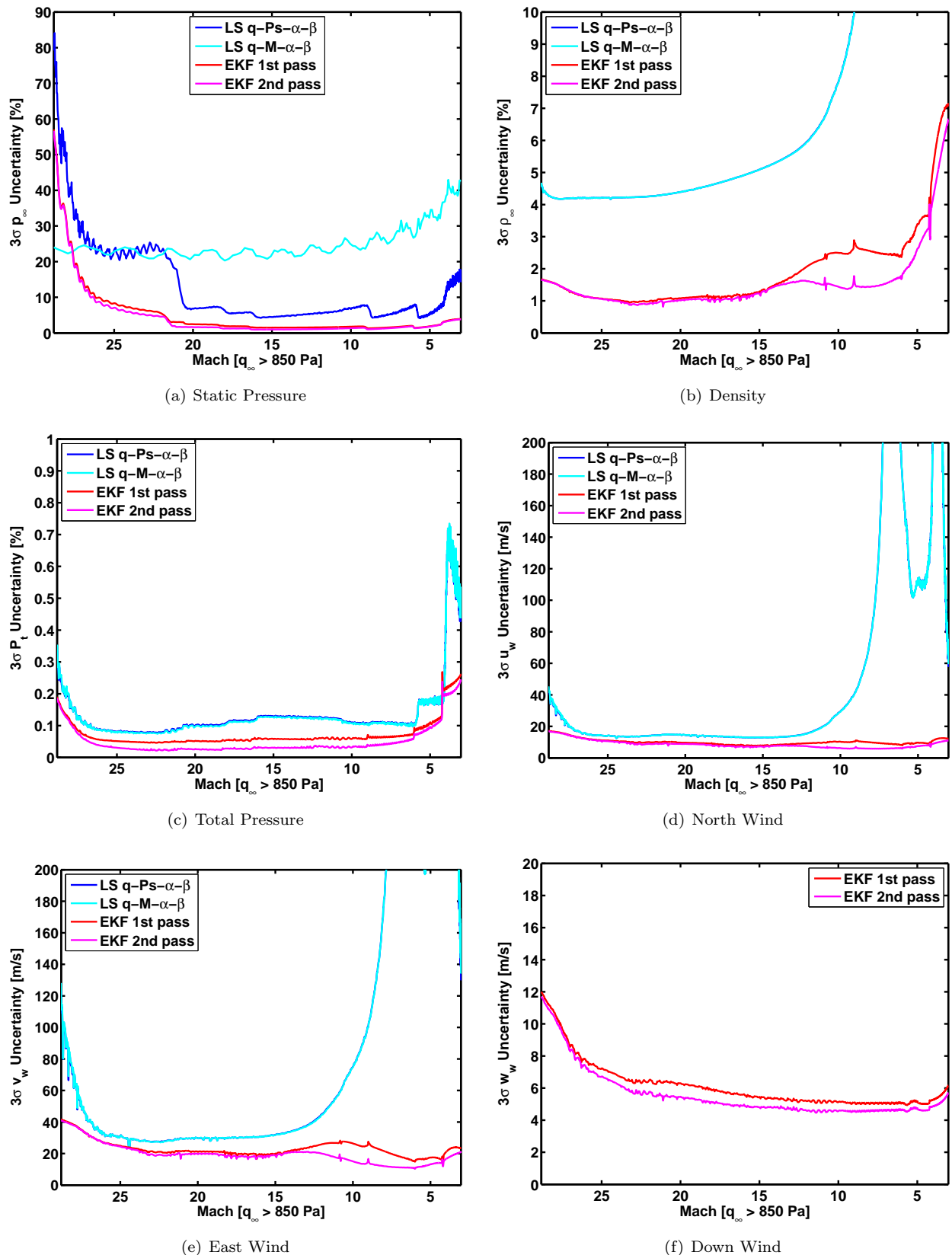


Figure 13. MEADS Secondary Science Objectives

## Acknowledgements

The authors wish to thank David M. Bose for preliminary implementation of the high-fidelity tube response models and early project guidance, Artem A. Dyakonov for supplying the CFD pressure models and assistance with interpreting these data, Jeff A. Herath for assistance with modelling the SSE, and Tim Schott for conducting independent tube response model analysis.

## References

<sup>1</sup>Gazarik, M. J., Wright, M. J., Little, A., Cheatwood, F. M., Herath, J. A., Munk, M. M., Novak, F. J., and Martinez, E. R., "Overview of the MEDLI Project," IEEE 2008 Aerospace Conference, March 2008.

<sup>2</sup>Munk, M., Hutchinson, M., Mitchell, M., Parker, P., Little, A., Herath, J., Bruce, W., and Cheatwood, N., "Mars Entry Atmospheric Data System (MEADS): Requirements and Design for Mars Science Laboratory (MSL)," 6th International Planetary Probe Workshop, Atlanta, GA, June 2008.

<sup>3</sup>Pruett, C. D., Wolf, H., Heck, M. L., and Siemers, P. M., "Innovative Air Data System for the Space Shuttle Orbiter," *Journal of Spacecraft and Rockets*, Vol. 20, No. 1, 1983, pp. 61–69.

<sup>4</sup>Siemers, P. M., Wolf, H., and Flanagan, P. F., "Shuttle Entry Air Data System Concepts Applied to Space Shuttle Orbiter Flight Pressure Data to Determine Air Data – STS 1-4," American Institute of Aeronautics and Astronautics, AIAA Paper 83-018, January 1983.

<sup>5</sup>Siemers, P. M., Henry, M. W., and Eades, J. B., "Shuttle Entry Air Data System (SEADS) – Advanced Air Data System Results: Air Data Across the Entry Speed Range," *Orbiter Experiments (OEX) Aerothermodynamics Symposium*, NASA CP-3248, Part I, April 1995, pp. 49–78.

<sup>6</sup>Hampel, F. R., Ronchetti, E. M., Rousseeuw, P. J., and Stahel, W. A., *Robust Statistics: The Approach Based on Influence Functions*, Wiley, 1986, pp. 307–311.

<sup>7</sup>Crassidis, J. C. and Junkins, J. L., *Optimal Estimation of Dynamic Systems*, Chapman & Hall/CRC, Boca Raton, FL, 2004.

<sup>8</sup>Weiss, S., "Comparing Three Algorithms for Modeling Flush Air Data Systems," American Institute of Aeronautics and Astronautics, AIAA Paper 2002-0535, January 2002.

<sup>9</sup>Kelly, G. M., Findlay, J. T., and Compton, H. R., "Shuttle Subsonic Horizontal Wind Estimation," *Journal of Spacecraft and Rockets*, Vol. 20, No. 4, 1983, pp. 390–397.

<sup>10</sup>Kasich, D. C. and Cheng, P. Y., "Flush Port / Inertially Blended Air Data Estimator," American Institute of Aeronautics and Astronautics, AIAA Paper 91-0670, January 1991.

<sup>11</sup>Wagner, W. E., "Re-Entry Filtering, Prediction, and Smoothing," *Journal of Spacecraft and Rockets*, Vol. 3, No. 9, 1966, pp. 1321–1327.

<sup>12</sup>Wagner, W. E. and Serold, A. C., "Statistical Trajectory Estimation Programs: Utilization Report," NASA CR-66837, June 1969.

<sup>13</sup>Wagner, W. E. and Serold, A. C., "Formulation on Statistical Trajectory Estimation Programs," NASA CR-1482, January 1970.

<sup>14</sup>"SV-5D PRIME: Final Flight Test Summary," Martin Marietta, Engineering Report 14465, Denver, CO, September 1967.

<sup>15</sup>Jones, J. F., "Development and Performance Analysis of a Trajectory Estimator for an Entry Through the Martian Atmosphere," American Institute of Aeronautics and Astronautics, AIAA Paper 72-953, September 1972.

<sup>16</sup>Hopper, F. W., "Trajectory, Atmosphere, and Wind Reconstruction from Viking Entry Measurements," American Astronautical Society, AAS Paper 75-068, July 1975.

<sup>17</sup>Euler, E. A., Adams, G. L., and Hopper, F. W., "Design and Reconstruction of the Viking Lander Descent Trajectories," *Journal of Guidance and Control*, Vol. 1, No. 5, 1978, pp. 372–378.

<sup>18</sup>Sabin, M. L., "Linear Filtering of Ballistic-Entry Probe Data for Atmospheric Reconstruction," *Journal of Spacecraft and Rockets*, Vol. 12, No. 2, 1975, pp. 66–73.

<sup>19</sup>Compton, H. R., Blanchard, R. C., and Findlay, J. T., "Shuttle Entry Trajectory Reconstruction Using Inflight Accelerometer and Gyro Measurements," American Institute of Aeronautics and Astronautics, AIAA Paper 79-0257, January 1979.

<sup>20</sup>Compton, H. R., Findlay, J., Kelly, G., and Heck, M., "Shuttle (STS-1) Entry Trajectory Reconstruction," American Institute of Aeronautics and Astronautics, AIAA Paper 81-2459, November 1981.

<sup>21</sup>Rao, P. P., "Titan IIIC Preflight and Postflight Trajectory Analysis," *Journal of Guidance, Control, and Dynamics*, Vol. 7, No. 2, 1984, pp. 161–166.

<sup>22</sup>Karlaagard, C. D., Tartabini, P. V., Blanchard, R. C., Kirsch, M., and Toniolo, M. D., "Hyper-X Post-Flight Trajectory Reconstruction," *Journal of Spacecraft and Rockets*, Vol. 43, No. 1, 2006, pp. 105–115.

<sup>23</sup>Beck, R. E., "Flight Trajectory and Axial Force Coefficient Data Reduction Scripts for IRVE," Analytical Mechanics Associates, Inc., AMA Report 06-09, June 2006.

<sup>24</sup>Beck, R. E. and Karlgaard, C. D., "Ares I-X: Best Estimated Trajectory Uncertainty Predictions," Analytical Mechanics Associates, Inc., AMA Report 09-21, March 2009.

<sup>25</sup>Bergh, H. and Tijdeeman, H., "Theoretical and Experimental Results for the Dynamic Response of Pressure Measuring Systems," NLR-TR F.238, January 1965.

<sup>26</sup>Whitmore, S. A., "Frequency Response Model for Branched Pneumatic Sensing Systems," *Journal of Aircraft*, Vol. 43, No. 6, 2006, pp. 1845–1853.

<sup>27</sup>Whitmore, S. A. and Fox, B., "Improved Accuracy, Second-Order Response Model for Pressure Sensing Systems," *Journal of Aircraft*, Vol. 46, No. 2, 2009, pp. 491–500.

<sup>28</sup>Beck, R., Karlgaard, C., and O'Keefe, S., "Mars Entry Atmospheric Data System Post-Flight Data Analysis Tool: Modeling and Sensitivity Updates," Analytical Mechanics Associates, Inc., AMA Report 07-20, December 2007.

<sup>29</sup>Beck, R. and Karlgaard, C., "Summary of MEADS Error Model Enhancements," Analytical Mechanics Associates, Inc., AMA Report 08-01, February 2008.

<sup>30</sup>Whitmore, S. A. and Moes, T. R., "Measurement Uncertainty and Feasibility Study of a Flush Airdata System for Hypersonic Flight Experiment," NASA TM 4627, 1994.

<sup>31</sup>Kennard, E. H., *Kinetic Theory of Gases*, McGraw-Hill, New York, 1938, pp. 327–333.

<sup>32</sup>Knudsen, M., "Thermischer Molekulardruck in Röhren," *Annalen der Physik*, Vol. 83, 1927, pp. 797–821.

<sup>33</sup>Rasmussen, M., *Hypersonic Flow*, John Wiley & Sons, Inc., New York, 1994.

<sup>34</sup>Potter, J. L., "Correction of Measured Pressures to Account for Thermomolecular Flow in Orifices and Tubes: User Guide and Program," Analytical Mechanics Associates, Inc., NASA Contract No. NAS1-18935, October 1991.

<sup>35</sup>Potter, J. L., Kinslow, M., and Boylan, D. E., "An Influence of the Orifice on Measured Pressures in Rarefied Flow," 4th Symposium on Rarefied Gas Dynamics, de Leeuw, J. H. (Ed.), Vol. 2, 1966, pp. 175–194.

<sup>36</sup>Kinslow, M. and Arney, G. D., Jr., "Thermomolecular Pressure Effects in Tubes and at Orifices," AGARDograph 119, August 1967.

<sup>37</sup>Kinslow, M. and Potter, J. L., "Reevaluation of Parameters Relative to the Orifice Effect," 7th Symposium on Rarefied Gas Dynamics, Dini, D., (Ed.), Vol. 1, 1971, pp. 399–408.

<sup>38</sup>Siemers, P. M., Bradley, P. F., Wolf, H., Flanagan, P. F., Weilmuenster, K. J., and Kern, F. A., "Shuttle Flight Pressure Instrumentation: Experience and Lessons for the Future," NASA Langley Conference on Shuttle Performance: Lessons Learned, Hampton, VA, March 1983.

<sup>39</sup>Wolf, H., Flanagan, P. F., and Henry, H. W., "Shuttle Entry Air Data System Program Manual," Analytical Mechanics Associates, Inc., AMA Report 85-4, March 1985.

<sup>40</sup>Gibson, F. A., Henry, M. W., and Eades, J. B., Jr., "Shuttle Entry Air Data System (SEADS) Data Analysis: A Historical Perspective," Analytical Mechanics Associates, Inc., AMA Report 92-7, December 1992.

<sup>41</sup>Gibson, L. S. and Sealey, B. S., "Test and Evaluation of Pressure Transducers for a Reentry Vehicle Pressure Measurement System," 39th International Instrumentation Symposium, May 1993, pp. 1013–1030.

<sup>42</sup>Parker, P. A., Hutchinson, M. A., Mitchell, M., and Munk, M. M., "Strategic Pressure Measurement System Characterization of the Mars Entry Atmospheric Data System," 6th International Planetary Probe Workshop, Atlanta, GA, June 2008.

<sup>43</sup>Karlgaard, C., Siemers, P., White, B., and O'Keefe, S., "Mars Entry Atmospheric Data System Performance Analysis," Analytical Mechanics Associates, Inc., AMA Report 09-02, January 2009.

<sup>44</sup>Farrell, J. A. and Barth, M., *The Global Positioning System and Inertial Navigation*, McGraw-Hill, New York, 2000.

<sup>45</sup>Konefat, E. H. and Litty, E. C., "Mars Science Laboratory Descent Inertial Measurement Unit," JPL Report D-34226, MSL-476-1237, March 7th, 2006.

<sup>46</sup>Chapin, W. G., "Dynamic-Pressure Measurements Using an Electrically Scanned Pressure Module," NASA TM-84650, July 1983.

<sup>47</sup>Bruce, W. and Siemers, P. M., "Aerothermal Effects of the MEDLI/MEADS Pressure Ports on the MSL PICA Heatshield and Compliance with Requirements," MEDLI-0197, May 2009.